Received: 1 August 2023 | Revised: 15 January 2024 | Accepted: 15 January 2024

DOI: 10.1002/mrm.30036

RESEARCH ARTICLE

Magnetic Resonance in Medicine

The coax monopole antenna: A flexible end-fed antenna for ultrahigh field transmit/receive arrays

Lyanne M. I. Budé[1,2] | **Bart R. Steensma**[3] | **Irena Zivkovic**[2] | **Alexander J. E. Raaijmakers**[1,3]

[1] Department of Biomedical Engineering, Eindhoven University of Technology, Eindhoven, The Netherlands

[2]Department of Electrical Engineering, Eindhoven University of Technology, Eindhoven, The Netherlands

[3]Division of Imaging and Oncology, UMC Utrecht, Utrecht, The Netherlands

Correspondence
Alexander J. E. Raaijmakers, Department of Biomedical Engineering, Eindhoven University of Technology, Eindhoven, The Netherlands.
Email: a.j.e.raaijmakers@tue.nl

Funding information
None.

Abstract

Purpose: The coax monopole antenna is presented for body imaging at 7 T. The antenna is fed at one end, eliminating the possibility of cable-coil coupling and simplifying cable routing. Additionally, its flexibility improves loading to the subject.

Methods: Like the coax dipole antenna, an interruption in the shield of the coaxial cable allows the current to extend to the outside of the shield, generating a B_1^+ field. Matching is achieved using a single inductor at the distal side, and a cable trap enforces the desired antenna length. Finite difference time domain simulations are employed to optimize the design parameters. Phantom measurements are conducted to determine the antenna's B_1^+ efficiency and to find the S-parameters in straight and bent positions. Eight-channel simulations and measurements are performed for prostate imaging.

Results: The optimal configuration is a length of 360 mm with a gap position of 40 mm. Simulation data show higher B_1^+ levels for the coax monopole (20% in the prostate), albeit with a 5% lower specific absorbance rate efficiency, compared to the fractionated dipole antenna. The S_{11} of the coax monopole exhibits remarkable robustness to loading changes. In vivo prostate imaging demonstrates B_1^+ levels of 10–14 μT with an input power of 8 × 800 W, which is comparable to the fractionated dipole antenna. High-quality images and acceptable coupling levels were achieved.

Conclusion: The coax monopole is a novel, flexible antenna for body imaging at 7 T. Its simple design incorporates a single inductor at the distal side to achieve matching, and one-sided feeding greatly simplifies cable routing.

KEYWORDS

Engineering, RF coil arrays, ultrahigh field MRI

1 | INTRODUCTION

For MRI at ultrahigh field ($B_0 \geq 7$ T), the short wavelength of the B_1^+ (transmit) field causes strong RF attenuation and complex interference patterns, resulting in signal voids and potentially increased peak local SAR,[1] which is defined as the peak level of the local specific absorption rate (SAR), averaged over 10 g of human tissue. Because of this, the commonly used birdcage body coil cannot be used for body imaging. Multi-channel transmit arrays are used to be able to steer the B_1^+ field to the region of interest. These antennas are most often placed directly on the body because this leads to higher B_1^+ efficiency and lower interelement coupling. In the past years, multiple groups have worked on optimizing transmit B_1 arrays for body imaging at ultrahigh field strengths. In particular, dipole antennas have demonstrated attractive features as transmit array elements.[2–5] A commonly used dipole antenna for body imaging at 7 T is the fractionated dipole antenna.[3,6–9] When a loop antenna is compared to a dipole antenna, with dimensions of both antennas optimized for the same depth at interest, dipole antennas show a higher B_1^+ efficiency at depth and more uniform transmit and receive profiles in comparison to loop antennas.[10] While showing these favorable characteristics, the rigid structure of conventional dipole antennas does not adapt to the body surface curvature. This results in suboptimal intersubject variation in imaging performance.[11]

The use of coaxial cables as RF coils has seen extensive applications in MRI due to the flexibility and homogeneous current profiles. Zhang et al. introduced a glove coil as a high-impedance coil array for hand imaging at 3 T, consisting of coaxial cable loop coils, attached to a glove.[12] These coils are shown to be adaptive to movement and were demonstrated to exhibit lower coupling levels and better SNR compared to conventional loop coils. Ruytenberg et al. introduced a shielded-coaxial-cable coil as a transmit–receive element at 7 T.[13] This coil showed to be less sensitive to coupling and deformation than traditional loop coils. Nohava et al. introduced flexible multi-turn multi-gap coaxial RF coils at 3 T and 7 T, making it possible to choose a coil diameter that is optimal for an anatomical site.[14]

The previously discussed coaxial cable coil designs all utilize loop coils; however, van Leeuwen et al. recently published the "*coax dipole*", which is based on the same principles as coaxial cable loop coils but applied to the dipole antenna design. Presented as a transmit–receive element for ultrahigh field body imaging, the coax dipole consists of a coaxial cable with two interruptions in the shield and inductors at both distal ends of the antenna to avoid reflections.[11] This antenna has been proven to perform similarly to the fractionated dipole antenna in terms of SAR and B_1^+ efficiency and has the advantage that the antenna is fully flexible and less sensitive to intersubject variation in load.

Although the flexibility of the coax dipole is beneficial, dipole antennas in general have the disadvantage that the antenna is fed at the center. This means that for arrays with tight spatial constraints, the feeding cable has to be placed parallel to one of the conductive legs of the antenna, where longitudinal E-fields are particularly strong. This makes the configuration highly susceptible to the induction of currents on the shield of the feeding cable, opening the possibility for cable-coil coupling. To avoid such coupling, the feeding cable has to be placed carefully, making cable routing difficult. An elegant solution to overcome this drawback is to use a monopole antenna. Hong et al. and Woo et al. proposed designs of monopole antennas as an alternative for a dipole antenna, both as an array for head imaging at 7 T and 10.5 T, respectively.[15,16] However, these monopole antennas were made from rigid, copper wire conductors that did not have the flexibility and flat current profile advantages that coaxial cable coils have.

Therefore, in this work the coax monopole antenna (CMA) is introduced, which operates based on similar principles as the coax dipole antenna. It consists of a coaxial cable, with an interruption in the shield to ensure that the current flows to the outside of the shield. Remarkably, as results will show, only one inductor at the distal side of the antenna is sufficient for matching the antenna and avoiding reflections.

A series of simulations will be used to explore the optimal design parameters. Single channel elements are compared to the fractionated dipole antenna for reference, both in simulations and measurements. Simulations of a full array on a human model are performed, and finally, an eight-channel array is built for imaging of the prostate of a human subject.

2 | METHODS

The subsequent steps to arrive at the design of the CMA and evaluate its performance will be outlined in this section. First, an extensive series of finite difference time domain simulations was performed to find that the proposed concept is feasible using the optimal parameters that result from this study. Then, single-channel measurements were used to verify the simulations and evaluate the behavior of the CMA in terms of B_1^+ efficiency. Bench measurements were performed to evaluate the coupling of the CMA, both in straight and bent positions. Simulations of an eight-channel array were then used to find the SAR and B_1^+ distributions for a prostate imaging setup on a human model. Lastly, to assess its B_1^+ efficiency and

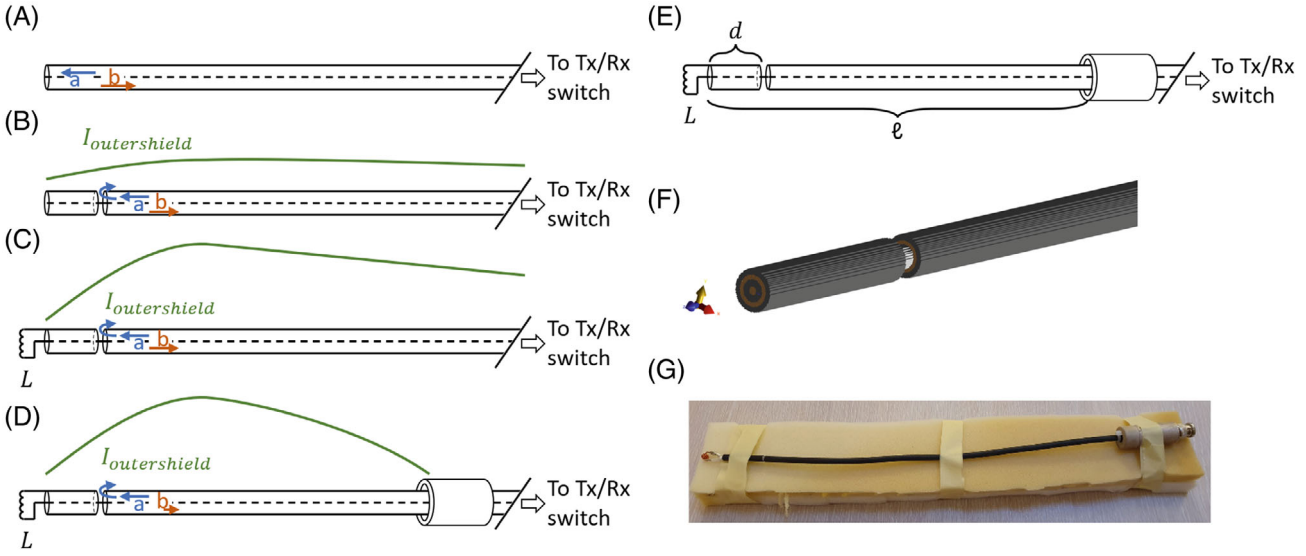

FIGURE 1 (A) Driving an open-ended coax cable gives full reflection and no current on the outside of the shield, and thus no B_1^+ field. (B) An interruption in the shield causes current to flow toward and on the outside of the shield, however, with very low amplitude because of full reflection. (C) An inductor at the end of the cable minimizes reflection, but the current on the outside propagates along the cable too far. (D) A cable trap forces the outside current to zero. (E) Optimization parameters. (F) Simulation grid of the antenna. (G) Photograph of coax monopole antenna on flexible foam substrate.

for proof-of-principle image acquisition, in vivo prostate imaging was performed using an eight-channel array of CMAs at 7 T. Where possible, the fractionated dipole antenna was used for comparison.[3]

2.1 | Design

A schematic depiction of the CMA is presented in Figure 1. This layout is based on the same principles as the coax dipole antenna. A series of images is used to clarify its working mechanism. First, driving the open-ended coax cable results in the absence of a current on the outside of the shield because there is only an incident current wave on the core of the coaxial cable, and a mirror current on the inside of its shield (Figure 1A). By introducing an interruption in the shield of the coaxial cable, the current will flow along the gap's edges toward the outside of the shield, thereby creating a magnetic field surrounding the antenna (Figure 1B). However, this current magnitude is very small because the vast majority of power is reflected. An obvious choice would be to add a matching network between the driving cable and the CMA. However, as results will show, it suffices to place an inductor at the CMA's ending to match the antenna to 50 Ω (Figure 1C).

On the outside of the shield of the coaxial cable, the current can propagate freely over the feeding cable. Instead of attenuating quickly, the current extends toward the feeding cable and shows a standing current wave. This means that the whole feeding cable becomes an antenna, in theory extending all the way to the amplifier. To prevent this, a 7 T ceramic cabletrap (Philips Healthcare, Best, The Netherlands) is placed around the antenna to force down the current at the desired position, enforcing a specific antenna length, as shown in Figure 1D. Figure 1E schematically depicts the parameters that need to be optimized.

2.2 | Single-channel simulations

To find the optimal parameters, a series of single-channel finite difference time domain simulations were performed in Sim4Life v7.2 (Zurich Medtech, Switzerland). The dimensions of the coaxial cable were modeled after a commercially available coaxial cable (Huber Suhner RG223u, characteristic impedance: 50 Ω). The coaxial cable's core and shield were modeled as a perfect electrical conductor. The outer diameters of the core, dielectric, shield, and jacket were set to 0.89, 2.95, 3.85, and 5.3 mm, respectively. The relative permittivity of the dielectric and the jacket were set to $\varepsilon_r = 2.3$ and $\varepsilon_r = 4.0$, respectively, to mimic the properties of a real coaxial cable. Both for the dielectric and the jacket, a conductivity of 0 S/m was used. The source was placed between the shield and the core of the coaxial cable.

Measured from the center of the antenna, the antenna was positioned 25 mm above a homogeneous phantom ($\sigma = 0.5$ S/m, $\varepsilon_r = 46$) with dimensions of $200 \times 300 \times 600$ mm^3. The antenna was then voxelized at a resolution of 2 mm in the z-direction and 0.15 mm in the x-y direction, ensuring sufficiently accurate voxelization of the

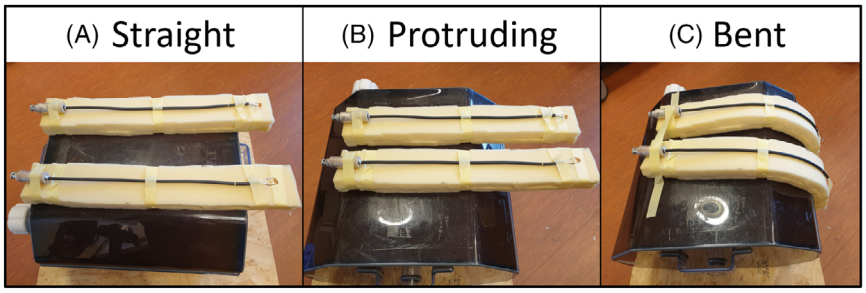

FIGURE 2 To evaluate the S-parameters and B_1^+ efficiency for various loading scenarios, three measurement setups were investigated. (A) On-phantom: the antennas are placed flat on the phantom. (B) Protruding: the antennas extend over the edge of the phantom. (C) Bent: the antennas are bent over the edge of the phantom.

circular structure of the antenna, as shown in Figure 1F. The phantom was voxelized at a maximum resolution of $5 \times 5 \times 5\,mm^3$. A total of 4.978–6.213 Mcells (1 Mcell = 1.0 $\times 10^6$ cells) was needed, depending on antenna length ℓ. A convergence criterion of −50 dB was used.

A combination of the length ℓ and gap position d had to be found such that it is possible to match the antenna to 50 Ω with a physically realizable inductor value L at the ending of the antenna. Investigated gap positions were 40, 60, 80, and 100 mm, and the length of the antenna was set to 300, 350, 400, 450, or 500 mm. For each combination of d and ℓ, a range of inductor values L was evaluated. By using network co-simulations, it is possible to evaluate a range of values for L without the need to run a simulation for each separate value.[17] After finding the optimal parameters for ℓ, d, and L, the B_1^+ and SAR distributions were extracted from Sim4Life.

2.3 | Phantom measurements

Two CMAs were constructed with optimal parameters as found from the simulation study. These antennas were used to evaluate the S_{11} and S_{21} parameters of the CMA. To evaluate the advantage of a flexible antenna, three setups were considered, as illustrated in Figure 2.

2.3.1 | On-phantom

The antennas are placed flat onto a homogeneous phantom (polyvinylpyrrolidone,[18] $\sigma = 0.5$ S/m, $\varepsilon_r = 46$).

2.3.2 | Protruding

Half of the antennas are placed over the edge of the phantom, whereas the other half are placed over the edge, in a straight position.

2.3.3 | Bent

The antennas are bent over the edge of the phantom.

The distance between the antennas is varied between 7 and 20 cm with increments of 1 cm.

One CMA was used to acquire B_1^+ maps (AFI[19] with flip angle (FA)/TE/TR1/TR2 = 65°/2.6/50/250 ms) on the phantom at 7 T (Achieva, Philips Healthcare, Best, The Netherlands). These maps were acquired for the three setups mentioned above. The on-phantom B_1^+ map was used to validate the simulations. The B_1^+ maps of the protruding and bent setups were used to evaluate the advantage of a flexible antenna over a rigid antenna. These measurements were carried out with the coax dipole and fractionated dipole antennas as well, for comparison.

2.4 | Eight-channel simulations

Eight-channel simulations were performed for prostate imaging. An array of eight CMAs was created and placed around Duke from the Virtual Family.[20] The resulting B_1^+ and SAR distributions were compared with a similar simulation using fractionated dipoles. The antennas were voxelized at a resolution of 0.15 mm in the x-y direction and 2 mm in the z-direction, whereas the human model was voxelized at a maximum resolution of $2.5 \times 2.5 \times 2.5\,mm^3$. A convergence criterion of −50 dB was used.

2.5 | In vivo measurements

An array of eight CMAs was constructed for prostate imaging, as shown in Figure 3. Each anterior element was placed on a 2.5 cm thick flexible foam so that the antennas can shape to the volunteer's body (Figure 3A). The posterior elements were placed in rigid foam casings to ensure a constant distance of 2.5 cm to the body (Figure 3B). An additional layer of foam ensures that the antenna does not move inside the casing. Note that its rigidity does not compromise loading of the coil because the body will shape to this casing. The setup for prostate imaging is shown in Figure 3C. The array was characterized by the S-parameter matrix, B_1^+ maps (AFI[19] with FA/TE/TR1/TR2 = 65°/2.6/50/250 ms), and T_2 weighted (T_2w) prostate imaging. The parameters for the T_2w images were as follows: turbo spin echo (TSE) with TSE factor 17, FA/TE/TR = 90°/90/5000 ms,

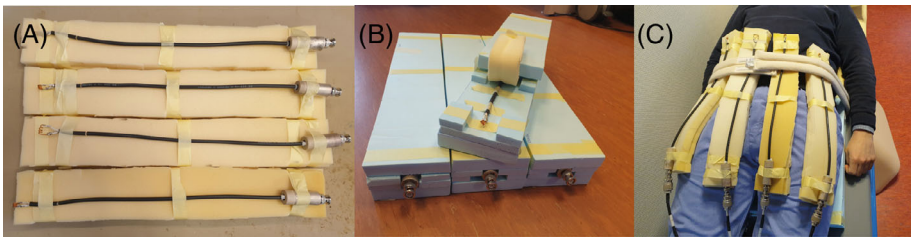

FIGURE 3 (A) Four coax monopole antennas, mounted on a flexible foam substrate to ensure flexibility (B) Four coax monopole antennas, encased in a rigid foam block. (C) Positioning of the antennas for prostate imaging.

FOV $250 \times 422 \times 44\,mm^3$, voxel size $0.7 \times 0.7 \times 3\,mm^3$. Subject-specific RF phase shimming on the prostate and parallel imaging (SENSE factor 1.5 in the left-right direction) was used. Measurements were performed on three male volunteers (age 23–44, body mass index 19–26); written informed consent was acquired before each measurement.

3 | RESULTS

3.1 | Single-channel simulations

For each combination of the length and gap position, reflection plots and Smith charts were created for a range of inductor values to evaluate the behavior of the CMA. Figure 4 shows results for nine combinations of the length and gap position, each evaluated using a range of inductor values. The rows represent the investigated lengths of the antenna, corresponding to 300, 350, and 400 mm, whereas each column shows a different gap position, corresponding to 40, 60, and 80 mm. The results of all tested combinations can be found in Figure S1. The combination of ℓ and d determines whether it is possible to match the antenna to 50 Ω by using only one inductor at the ending of the antenna. The resulting Smith charts show that a combination of $d = 40$ mm and $\ell = 350$ mm enables matching the antenna using an inductance of 39.5 nH. The corresponding reflection plots show that this value for L will indeed minimize reflections.

For these optimal design parameters, antenna field distributions were evaluated. In Figure 5A,B, the simulated 10 g averaged SAR distributions and B_1^+ distributions are shown, both for the CMA (top) and fractionated dipole (bottom). Peak local SAR levels were 1.10 W/kg for the CMA and 0.686 W/kg for the fractionated dipole for 1 W input power. The longitudinal B_1^+ profile of the CMA, taken along the green line of Figure 5B, is skewed in the direction of the gap but is also wider and higher than the profile of the fractionated dipole, as shown in Figure 5D. The maximum B_1^+ values at 5 cm depth were 0.62 μT (CMA) and 0.49 μT (fractionated dipole), resulting in a 27% higher B_1^+ efficiency for the CMA, in comparison to the fractionated dipole antennas. The in-depth B_1^+ profiles of the two antennas, measured at the maximum, as indicated by the red lines of Figure 5B, are shown in Figure 5G. Here, it is shown that the CMA has a higher B_1^+ field over the whole depth of the phantom.

3.2 | Antenna construction

The CMA was constructed by placing a cabletrap at the connector of the piece of coaxial cable and measuring ℓ and d from the end of the cabletrap. The hand-wound inductor at the end of the coaxial cable was connected between the shield and the core. Several iterations with slight changes in the length and gap position have been performed to arrive at a matched configuration. The resulting parameters were a length of 360 mm and a gap position of 40 mm. A picture of the CMA, as realized using this procedure, is shown in Figure 1G.

3.3 | Phantom measurements

Figure 5C shows the B_1^+ distributions for the single-channel phantom measurements using the CMA (top) and fractionated dipole (bottom). The B_1^+ efficiency along the longitudinal profile at 5 cm depth, as measured along the green lines in Figure 5C, is indicated in Figure 5F. The in-depth B_1^+ profiles, as measured along the red lines in Figure 5C, are shown in Figure 5G. These profiles show the similarity between the fractionated dipole and CMA.

Figure 6A shows the S_{11} parameters of the CMA, coax dipole, and fractionated dipole for the three investigated loading setups. The on-phantom, protruding, and bent setups are indicated by the green, orange, and blue lines, respectively. The bent setup is only considered for the CMA and coax dipole due to the rigidity of the fractionated dipole. Figure 6A shows that for the CMA the reflections remain below −9.7 dB at 298 MHz for all setups, whereas the resonance frequency of the CMA shifts less than 1 MHz. For the coax dipole antenna, the resonance frequency shifted up 13 MHz for the protruding case, and the reflection increases from −14.1 to −4.8 dB at 298 MHz. By bending the coax dipole over the edge, the resonance frequency returned close to the original frequency but with

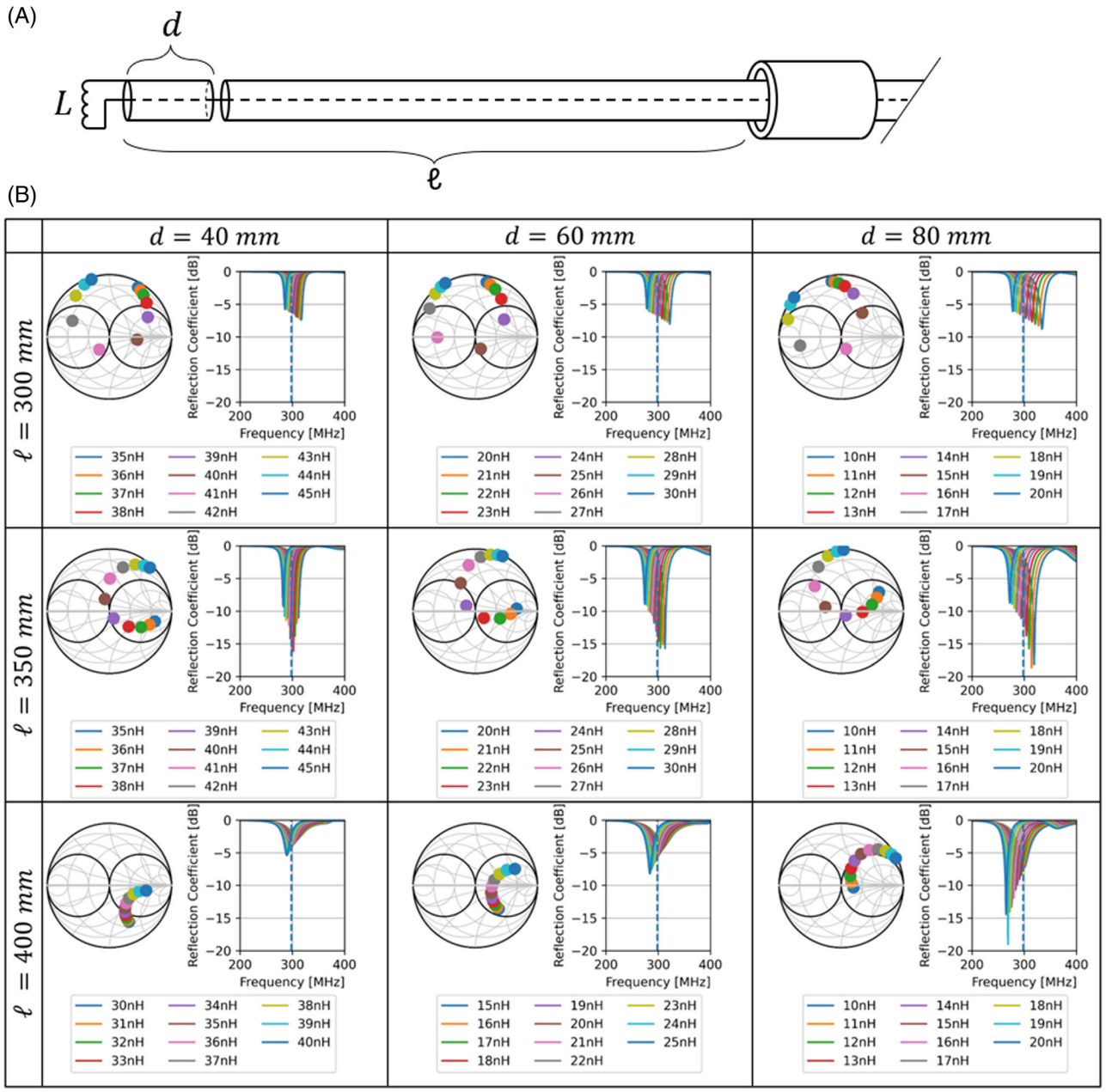

FIGURE 4 (A) Definition of optimization parameters. (B) Reflection plots and Smith-charts for different combinations of the monopole length, gap position, and inductance. Each row represents a specific antenna length, whereas each column shows a different gap position. For every combination of these, the dependence of reflection and impedance on L is investigated. Choosing a length of 350 mm and a gap position of 40 mm makes it possible to match the antenna with an inductance of 39.5 nH.

a 4.7 dB higher reflection. As for the fractionated dipole, the resonance frequency shifted 26 MHz when the antenna is protruding over the edge of the phantom and the reflection increased from −19.9 to −7.7 dB at 298 MHz.

Figure 6B shows the S_{21} parameters of the CMA, coax dipole, and fractionated dipole antennas for the on-phantom setup. The CMA showed higher interelement coupling than the two dipole antennas (−12.4 dB vs. −15.4 and −15.1 dB at 10 cm interelement distance). Figure 6C shows the S_{21} parameters for the protruding and bent setups. The S_{21} parameters of all three antennas increased with 3.0 dB (CMA), 1.5 dB (coax dipole), and 2.6 dB (fractionated dipole) when the antennas were protruding, compared to the on-phantom setup. However, the coupling for the CMA and coax dipole antenna decreased again to their original coupling parameters when the antennas were bent over the phantom edge.

In Figure 7A, B_1^+ measurements are shown for the protruding and bent setups. Taking the B_1^+ profile at 5 cm depth, measured along the green line, results in the profiles

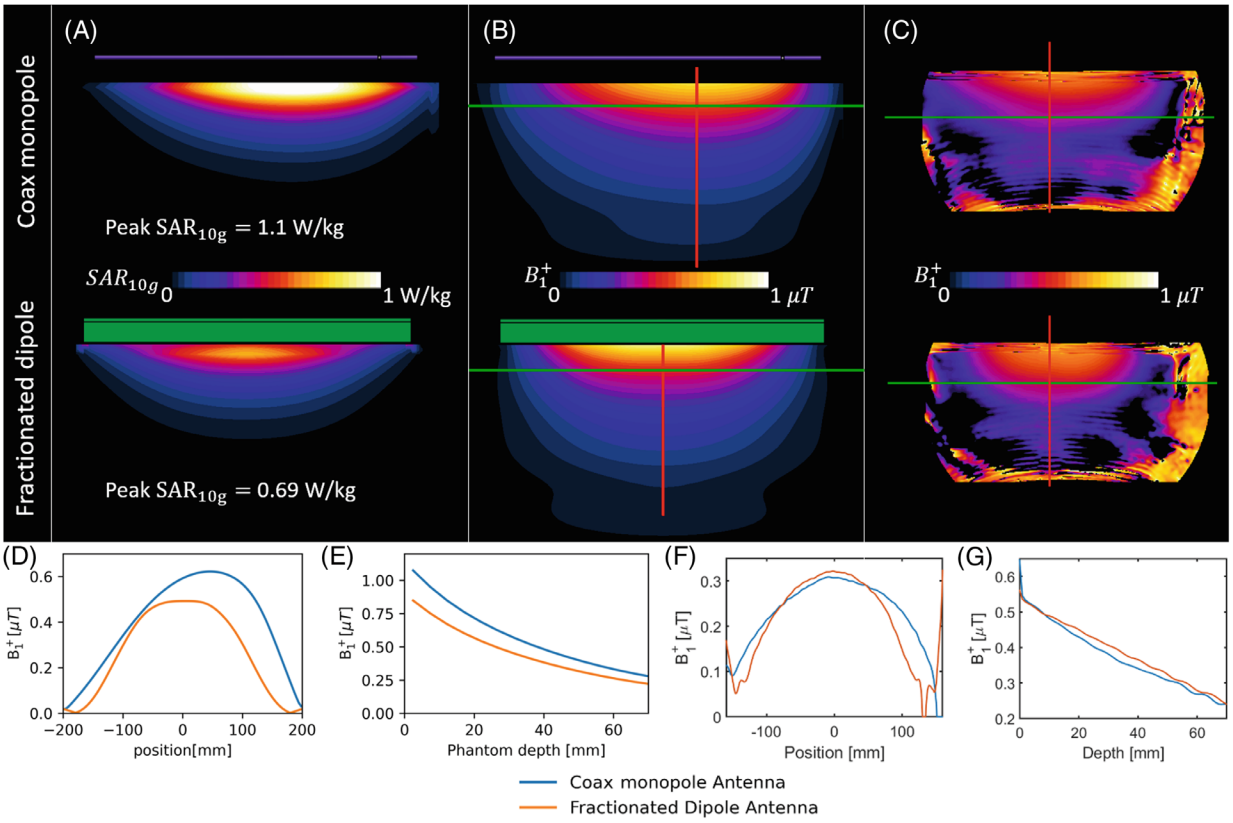

FIGURE 5 (A–C) For coax monopole (top) and fractionated dipole (bottom), (A) simulated 10 g averaged SAR distributions, (B) simulated B_1^+ distributions, and (C) measured B_1^+ distributions in 7 T MRI. (D) Simulated longitudinal B_1^+ profiles at a depth of 5 cm (taken along the green lines in B). (E) Simulated in-depth B_1^+ profiles (taken along the red lines in B). (F) Measured longitudinal B_1^+ profiles at 5 cm depth (taken along the green lines in C). (G) Measured in-depth B_1^+ profiles (taken along the red lines in C). All distributions and profiles are normalized to 1 W input power. SAR, specific absorption rate.

as shown in Figure 7B. In Figure 7C, the depth profiles, measured along the blue lines, are depicted. These figures show the advantage of a flexible antenna. When considering only the on-phantom setup, the coax monopole outperformed the coax dipole antenna in terms of B_1^+. However, the fractionated dipole reached higher B_1^+ values than both coax antennas. In the bent position, the rigidity of the fractionated dipole antenna showed a clear disadvantage because both coax antennas now reach higher B_1^+ values than the fractionated dipole. The coax monopole showed higher penetration depth in comparison to the coax dipole.

3.4 | Eight-channel simulations

In Figure 8A, the simulation setup with eight elements on a human model is shown. Figures 8B,C show the B_1^+ and 10 g averaged SAR distributions for an array setup with eight elements on a human model, normalized to 8×1 W input power. The left column shows results for the CMA, whereas the right column shows the same results for the fractionated dipole, for comparison. For the CMA, higher B_1^+ values were found at the cost of higher peak SAR in comparison to the fractionated dipole. The average B_1^+ in the prostate and peak SAR_{10g} values were 0.78 μT and 3.67 W/kg (CMA), and 0.65 μT and 2.25 W/kg (fractionated dipole). The resulting $B_1^+/\sqrt{SAR_{10g}}$ ratio in the prostate was 0.41 $\mu T/\sqrt{W/kg}$ for the CMA and 0.43 $\mu T/\sqrt{W/kg}$ for the fractionated dipole antenna.

3.5 | In vivo measurements

Reflection and interelement coupling were acceptable for three volunteers, as shown in Figure 9. The B_1^+ maps for three male volunteers are shown in Figure 10A. B_1^+ levels within the prostate were 10, 12, and 14 μT for the three volunteers, whereas good-quality T_2w prostate images were acquired as shown in Figure 10B.

4 | DISCUSSION

In this work, the CMA has been presented as a flexible antenna for body imaging at 7 T. The design of this antenna is based on the same principles as the coax dipole antenna

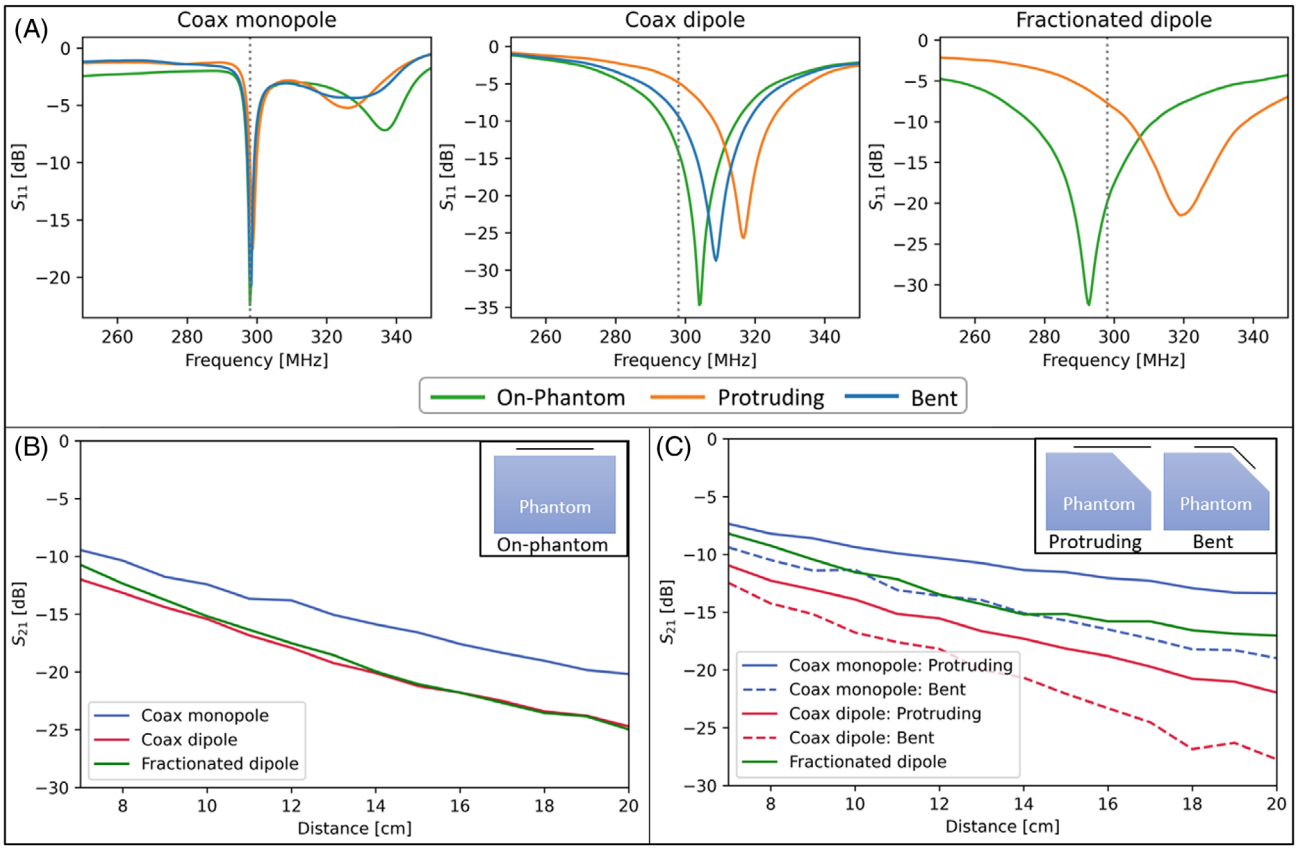

FIGURE 6 (A) S_{11} measurements for the coax monopole, coax dipole, and fractionated dipole for three setups. (B) S_{21} parameters for the coax monopole, coax dipole, and fractionated dipole, where the antennas are placed flat on the phantom. (C) S_{21} parameters for the coax monopole, coax dipole, and fractionated dipole, where the antennas extend over the edge of the phantom. For the coax monopole and coax dipole, the antennas are bent over the edge of the phantom as well.

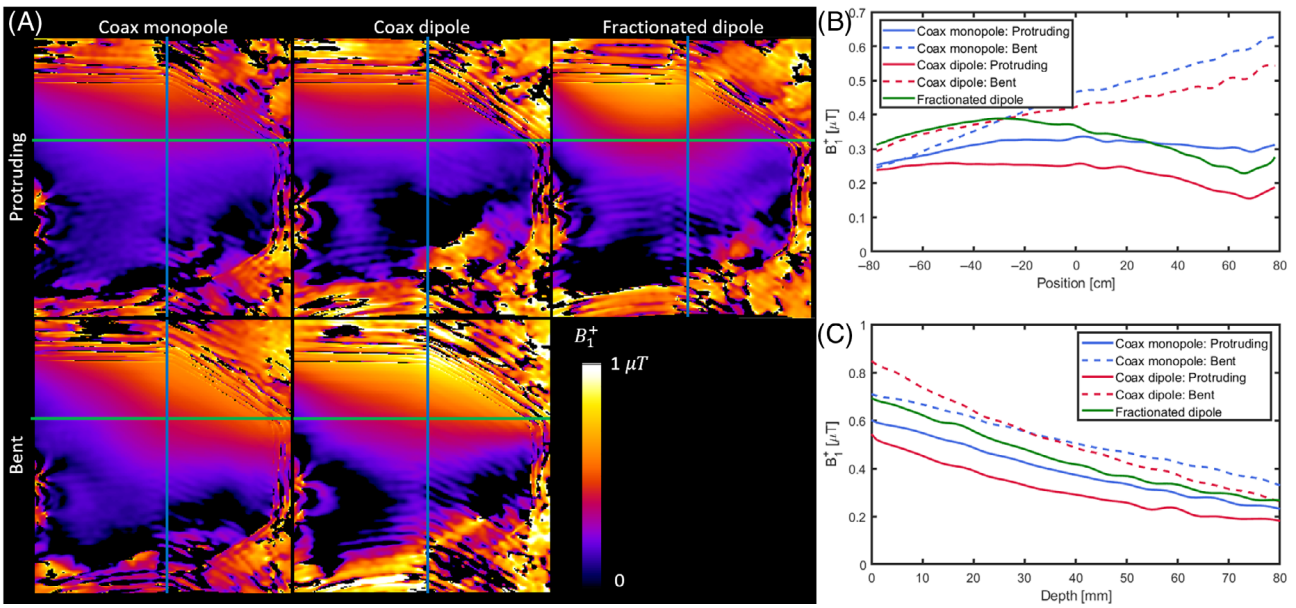

FIGURE 7 (A) B_1^+ maps of the single channel measurements for the antennas over the edge of the phantom in straight (row 1) and bent (row 2) position. (B) B_1^+ profiles at 5 cm depth along the green lines. (C) B_1^+ profiles along the blue lines.

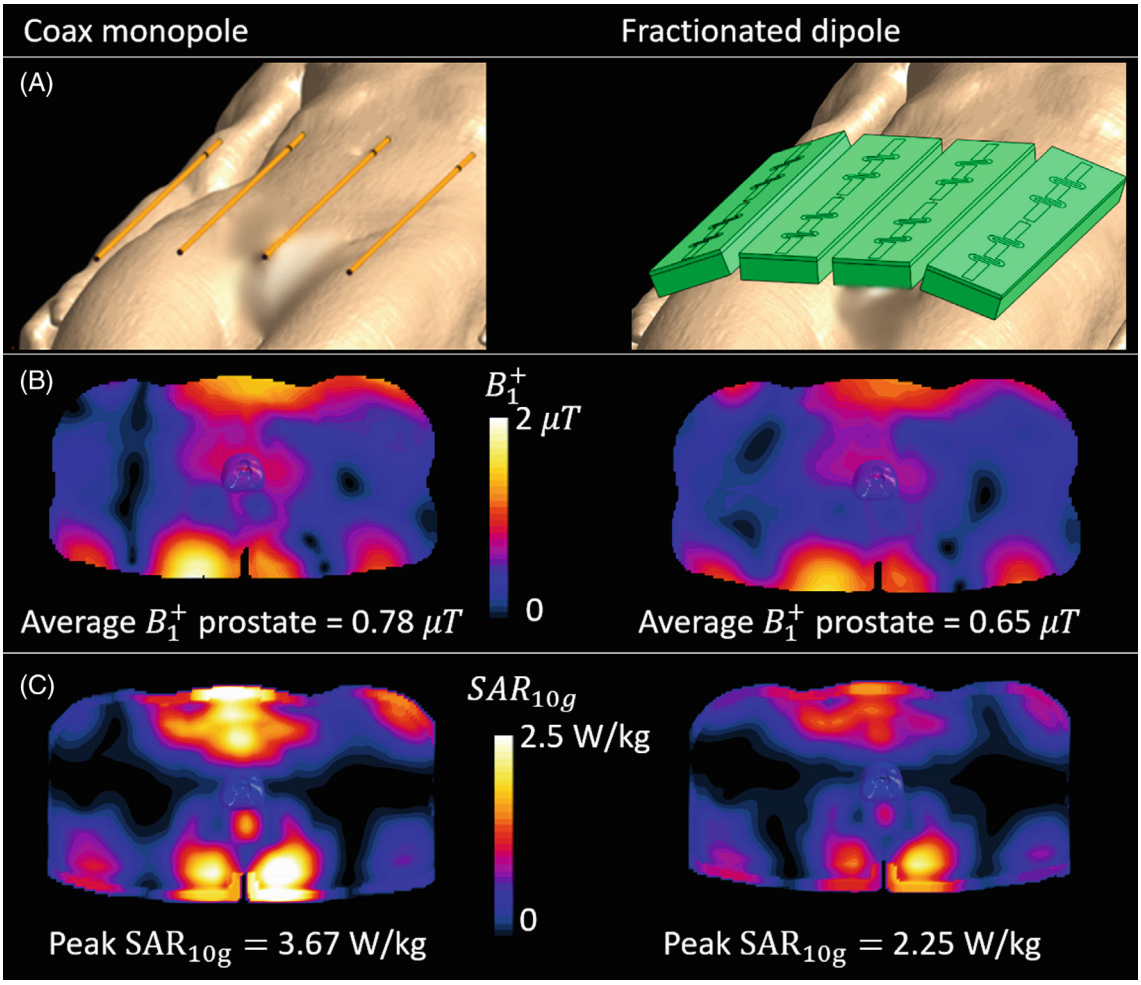

FIGURE 8 (A) Eight-channel simulation setup for prostate imaging. (B) B_1^+ distributions and (C) SAR distributions, all for the coax monopole antenna on the left and fractionated dipole on the right. The results are normalized to 8 × 1 W input power.

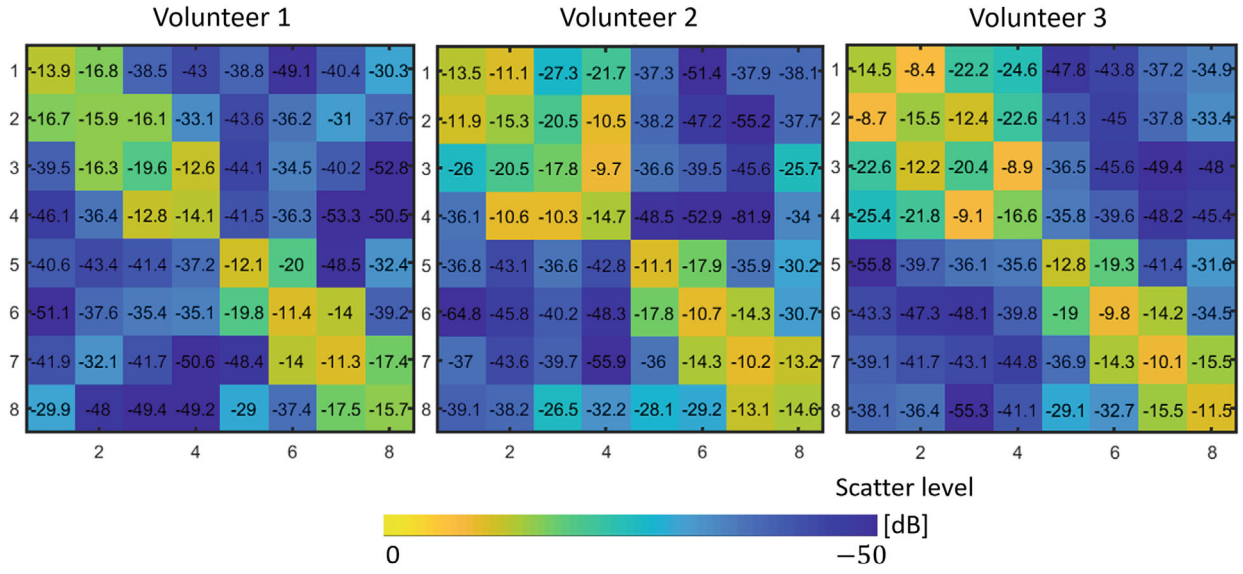

FIGURE 9 S-matrices of the eight-channel coax monopole array for three volunteers with a BMI of 26 (volunteer 1), 19 (volunteer 2), and 20 (volunteer 3). BMI, body mass index.

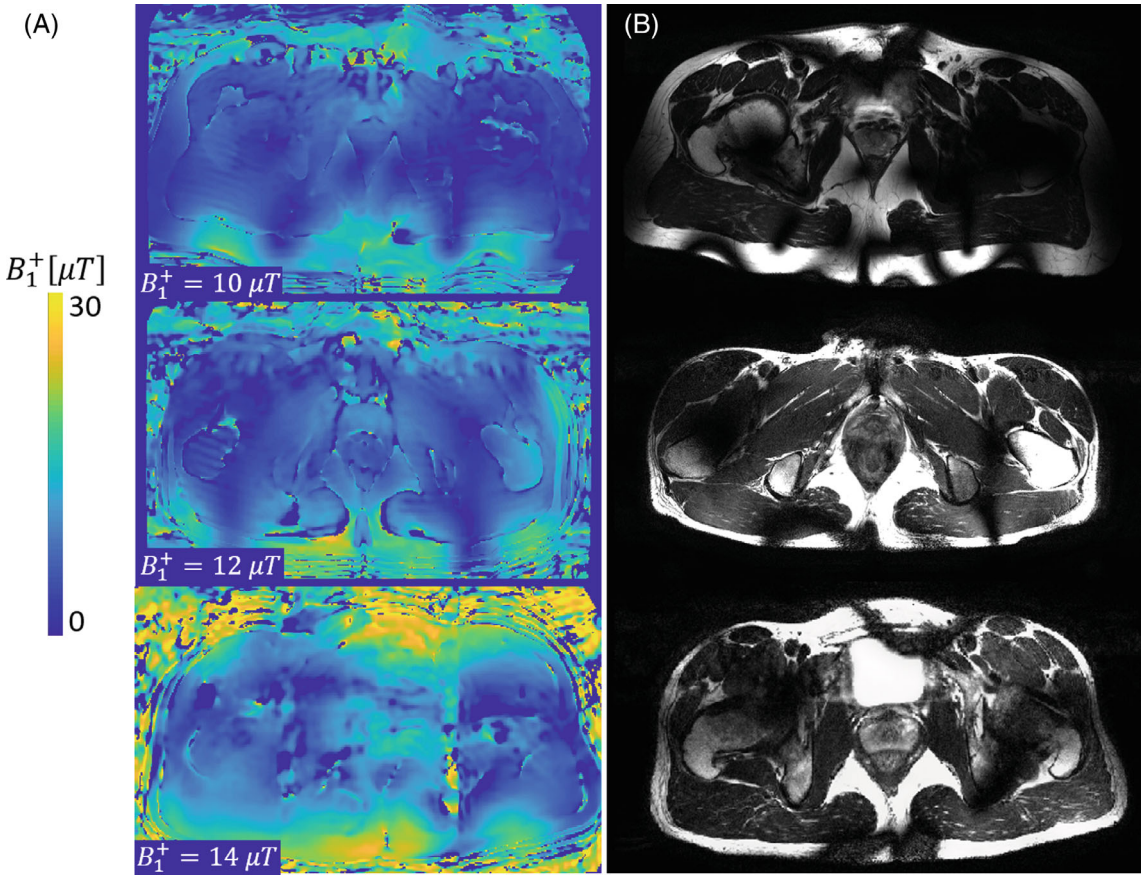

FIGURE 10 (A) B_1^+ map of the prostate for three volunteers (AFI[19] with FA/TE/TR_1/TR_2 = 65°/2.6/50/250 ms) input power = 8 × 800 W. (B) T_2w image of the prostate for three volunteers (TSE with TSE factor 17, FA/TE/TR = 90°/90/5000 ms, FOV 250 × 422 × 44 mm^3, voxel size 0.7 × 0.7 × 3 mm^3. Subject-specific RF phase shimming on the prostate and parallel imaging [SENSE factor = 1.5] was used). FA, flip angle; T_2w; T_2 weighted; TSE, turbo spin echo.

and coax loop coils.[11–14] The current running on the inside of the shield of the coaxial cable, as a reaction to the current on the core, can extend to the outside of the shield by creating an interruption in the shield. This outside-shield current generates the B_1^+ field. Matching of the antenna is achieved by placing an inductor between the shield and the core of the coaxial cable at the distal side of the antenna.

The CMA addresses the drawback of dipole antennas in general, where the antenna is fed at the center. The feeding cable has to be placed parallel to one of the legs of the antenna, where the electric fields are particularly high. This leads to the risk of cable-coil coupling and makes cable routing more difficult, especially in space-constrained coil configurations. The CMA, however, is fed at only one side, eliminating the possibility for cable-coil coupling and thereby greatly facilitating cable management.

To illustrate the disadvantageous effect of cable-coil coupling, a small experiment was performed, where a fractionated dipole antenna is placed on the aforementioned body phantom. Three setups were considered: (1) the feeding cable is routed perpendicularly and away from the antenna; (2) the feeding cable is routed parallel and is attached to the side of the housing of the antenna; and (3) the feeding cable is routed parallel and is attached to the top of the housing of the antenna as a worst-case scenario. All setups are depicted in Figure S2A. B_1^+ maps of these situations, which can be found in Figure S2B, show that the B_1^+ field distribution changes and deviates from what is expected from simulation studies. This interaction can also cause the peak SAR location and value to change, which makes accurate SAR predictions difficult. Although setup three seems to indicate a higher B_1^+ efficiency, the B_1^+ distribution becomes skewed, with lower B_1^+ levels at the side where the feeding cable is routed. Note that the fractionated dipole antenna was optimized for a high B_1^+ and SAR efficiency at deeply located tissues, so deviations from the intended behavior are likely to result in disadvantageous effects. On top of this, this experiment was carried out on a body phantom, which causes heavy loading of the antennas. Larger difficulties are expected in arrays where the antennas are loaded with a lighter load, such as head

arrays, especially in arrays with tight spatial constraints because of, for example, an insert gradient.

Although the experiments were performed using a fractionated dipole antenna, we expect the same behavior for coax dipole antennas. The current distributions on the outside of the shield of the coax dipole antenna are comparable to those of the fractionated dipole antenna; therefore, similar field distribution distortions are expected for the coax dipole antenna.

The influence of cable-coil coupling has also been investigated by Woo et al. In this research, an eight-channel dipole array was used for head imaging at 10.5 T, where the feeding cable was placed at 7 and 2 cm away from the antennas. In their simulation geometry, as well as in their measurements, cable traps were placed over the feeding cable to reduce sheath currents. Even with the presence of these cable traps, the B_1^+ efficiency was found to be 20.7% higher when the feeding cable was routed at further distance from the antenna.[21]

The CMA is matched by a single inductor at the distal side of the antenna. This is similar to the coax dipole antenna, where inductors are used at both endings of the antenna to reduce reflections.[11] To be more precise, the piece of coaxial cable beyond the gap transforms the impedance of the inductor to an impedance at the gap that effectively matches the antenna; that is, it minimizes reflections at the coax cable–gap transition.

It could be argued that the CMA, as presented in this work, is not a typical monopole antenna. A classical monopole antenna consists of one conductor rod with a ground plane underneath. However, monopole antennas come in many different layouts. Antennas like the top-loaded monopole antenna,[22] box-shaped loaded monopole,[23] and folded unipole antennas[24] are considered monopole antennas, although these are not traditional monopole antennas. Because the CMA is fed at one side, the term *coax monopole antenna* will be used for the sake of clarity.

Single-channel simulations show increased B_1^+ levels distributed over a larger FOV at the cost of higher peak SAR levels in comparison to the fractionated dipole. This is also found in eight-channel simulations for prostate imaging. The SAR efficiency of the CMA is 5% lower than that of the fractionated dipole.

On the other hand, S-parameter measurements show that the CMA is very stable with respect to loading variations of the antenna. Protruding the antenna over the edge of a phantom and bending the antenna over the edge does not change the resonance frequency of the antenna. Both the fractionated dipole and the coax dipole antenna are much more susceptible to changes in loading of the antenna. For these antennas, the resonance frequency increases when extending them over the edge of the phantom. For the coax dipole, the resonance frequency shift is more limited after bending the antenna over the edge of the phantom. Strikingly, for the CMA, a resonance shift is completely absent both when protruding or bent over the edge.

Further investigation is required to determine the underlying factors contributing to the CMA's low sensitivity to changes in load. One potential explanation is related to the losses in the antenna. In simulations, the B_1^+ efficiency of the CMA is higher than for the fractionated dipole, although the B_1^+ efficiency is the same for the two antennas in measurements, as illustrated in Figure 5. This indicates higher losses in the CMA than in the fractionated dipole antenna. The difference in B_1^+ efficiency in the simulations and measurements may be explained by the assumption of perfect conductors and zero conductivity of the jackets and the dielectric, whereas in practice losses occur in these components. Because the losses of the antenna increase, the susceptibility to loading effects is decreased. When simulating a setup that is similar to the protruding setup, a resonance shift is found for the coax monopole antenna. This strengthens our hypothesis that the absence of this shift is caused by the losses in the antenna, because the simulation is completely loss-free. However, the robustness to loading variations seems stronger than could be explained by somewhat higher losses.

The CMA does, however, exhibit higher coupling levels to neighboring elements in comparison to the coax dipole and fractionated dipole antennas, although these levels are not dramatically high. When the antennas are placed on the body of the volunteer, coupling levels are comparable to levels that are found for the fractionated dipole antenna.[3] The higher coupling levels for volunteers 2 and 3 can be explained by the variation in pelvic circumference of the three volunteers, which were 104, 83, and 82 cm, respectively. The smaller circumference of the second and third volunteer forces the elements to be placed closer together than for volunteer 1. The average inter-element distance was 12.5 cm for volunteer 1, and 10 cm for volunteers 2 and 3, leading to higher coupling levels.

The benefit of the flexibility of the antenna is demonstrated by single-channel measurements where the antenna is protruding or bent over the edge of a body phantom. B_1^+ levels increase significantly when the antenna is bent over the edge because this leads to proper loading of the antenna, and the B_1^+ field is focused toward the phantom. In addition, the coil's flexibility increases subject comfort.

Prostate imaging for three subjects shows high quality T_2w images. B_1^+ values of 10–14 μT are found in the prostate with a forward power of 8×800 W. This results

in levels that are comparable to the coax dipole antenna and fractionated dipole antenna, which mention levels of 11–14 μT and 7–15 μT at the same forward power, respectively.[3,11]

When the CMA would be used as receive elements, the SNR would be proportional to the transmit efficiency of the CMA. Because of the higher interelement coupling, it could be expected that the G-factor of the CMA is higher than the G-factor of the fractionated dipole and coax dipole antennas. However, a full investigation on the performance of the CMA in receive mode has not been performed because the expectation is that the CMA will likely be used as a transmit array. Typically, an array of CMAs would be combined with a second (loop coil) array, designated for receive only.

In future work, imaging sites other than the prostate will be evaluated. Particularly head coil arrays with tight space constraints (e.g., when combined with an insert gradient) will benefit from the easier cable routing for the CMA. Also, more benefits are expected for imaging sites with irregularly shaped surfaces where sufficient loading of rigid antennas is more challenging. Intersubject variation is expected to be minimized; the coil is always properly loaded because it shapes to the subject's body.

5 | CONCLUSION

The coax monopole antenna has been introduced as a novel antenna for body imaging at 7 T. Simulations show that this antenna has a higher B_1^+ efficiency (20% in the prostate) at the cost of a 5% lower SAR efficiency in comparison to the fractionated dipole antenna. The end-feeding of the CMA greatly facilitates cable routing in comparison to a dipole antenna, where the feeding cable often needs to run parallel to one of the antenna legs. A striking feature of the CMA is that this antenna uses only one matching element at the distal side of the antenna. Similar to the coax dipole antenna, the flexibility of the CMA shows benefits over rigid coils.

ORCID

Lyanne M. I. Budé https://orcid.org/0009-0009-0507-9890
Bart R. Steensma https://orcid.org/0000-0002-4254-9937
Irena Zivkovic https://orcid.org/0000-0001-6900-6580
Alexander J. E. Raaijmakers https://orcid.org/0000-0001-7111-330X

REFERENCES

1. Vaughan JT, Snyder CJ, DelaBarre LJ, et al. Whole-body imaging at 7T: preliminary results. *Magn Reson Med*. 2009;61:244-248.
2. Raaijmakers AJE, Ipek O, Klomp DWJ, et al. Design of a radiative surface coil array element at 7 T: the single-side adapted dipole antenna. *Magn Reson Med*. 2011;66:1488-1497.
3. Raaijmakers AJE, Italiaander M, Voogt IJ, et al. The fractionated dipole antenna: a new antenna for body imaging at 7 Tesla. *Magn Reson Med*. 2016;75:1366-1374.
4. Zivkovic I, Castro CA, Webb A. Design and characterization of an eight-element passively fed meander-dipole array with improved specific absorption rate efficiency for 7 T body imaging. *NMR Biomed*. 2019;32:e4106.
5. Steensma B, Moortele P, Ertürk A, et al. Introduction of the snake antenna array: geometry optimization of a sinusoidal dipole antenna for 10.5T body imaging with lower peak SAR. *Magn Reson Med*. 2020;84:2885-2896.
6. Sadeghi-Tarakameh A, Adriany G, Metzger GJ, et al. Improving radiofrequency power and specific absorption rate management with bumped transmit elements in ultra-high field MRI. *Magn Reson Med*. 2020;84:3485-3493.
7. Steensma BR, Voogt IJ, Leiner T, et al. An 8-channel Tx/Rx dipole array combined with 16 Rx loops for high-resolution functional cardiac imaging at 7 T. *MAGMA*. 2018;31:7-18.
8. Ertürk MA, Raaijmakers AJE, Adriany G, Uğurbil K, Metzger GJ. A 16-channel combined loop-dipole transceiver array for 7 Tesla body MRI. *Magn Reson Med*. 2017;77:884-894.
9. Ertürk MA, Wu X, Eryaman Y, et al. Toward imaging the body at 10.5 Tesla. *Magn Reson Med*. 2017;77:434-443.
10. Erturk MA, Li X, van de Moortele PF, Ugurbil K, Metzger GJ. Evolution of UHF body imaging in the human torso at 7T. *Top Magn Reson Imaging*. 2019;28:101-124.
11. van Leeuwen CC, Steensma BR, Klomp DWJ, van den Berg CAT, Raaijmakers AJE. The coax dipole: a fully flexible coaxial cable dipole antenna with flattened current distribution for body imaging at 7 Tesla. *Magn Reson Med*. 2022;87:528-540.
12. Zhang B, Sodickson DK, Cloos MA. A high-impedance detector-array glove for magnetic resonance imaging of the hand. *Nat Biomed Eng*. 2018;2:570-577.
13. Ruytenberg T, Webb A, Zivkovic I. Shielded-coaxial-cable coils as receive and transceive array elements for 7T human MRI. *Magn Reson Med*. 2020;83:1135-1146.
14. Nohava L, Czerny R, Roat S, et al. Flexible multi-turn multi-gap coaxial RF coils: design concept and implementation for magnetic resonance imaging at 3 and 7 Tesla. *IEEE Trans Med Imaging*. 2021;40:1267-1278.
15. Hong SM, Park JH, Woo MK, Kim YB, Cho ZH. New design concept of monopole antenna array for UHF 7T MRI. *Magn Reson Med*. 2014;71:1944-1952.
16. Woo MK, Delabarre L, Waks M, et al. Comparison of 16-channel asymmetric sleeve antenna and dipole antenna transceiver arrays at 10.5 Tesla MRI. *IEEE Trans Med Imaging*. 2021;40:1147-1156.
17. Beqiri A, Hand JW, Hajnal JV, Malik SJ. Comparison between simulated decoupling regimes for specific absorption rate prediction in parallel transmit MRI. *Magn Reson Med*. 2015;74:1423-1434.
18. Ianniello C, de Zwart JA, Duan Q, et al. Synthesized tissue-equivalent dielectric phantoms using salt and polyvinylpyrrolidone solutions. *Magn Reson Med*. 2018;80:413-419.
19. Yarnykh VL. Actual flip-angle imaging in the pulsed steady state: a method for rapid three-dimensional mapping of

the transmitted radiofrequency field. *Magn Reson Med*. 2007;57:192-200.
20. Gosselin MC, Neufeld E, Moser H, et al. Development of a new generation of high-resolution anatomical models for medical device evaluation: the virtual population 3.0. *Phys Med Biol*. 2014;59:5287-5303.
21. Woo MK, DelaBarre L, Waks MT, et al. Evaluation of 8-channel radiative antenna arrays for human head imaging at 10.5 Tesla. *Sensors*. 2021;21:6000.
22. Qu B, Pang Y, Wang L, Zhang A, Xu Z. Wideband Top-Loaded Monopole Antenna. *Proceedings: 2022 16th European Conference on Antennas and Propagation (EuCAP)*. New York, NY: Institute of Electrical and Electronics Engineers (IEEE); 2022:1-4.
23. Zivkovic I, Scheffler K. Single-channel, box-shaped, monopole-type antenna for B1+ field manipulation in conjunction with the traveling-wave concept in 9.4 T MRI. *MAGMA*. 2015;28:357-362.
24. Leonhard J, Mattuck R, Pote A. Folded unipole antennas. *IRE Trans Antennas Propag*. 1955;3:111-116.

SUPPORTING INFORMATION

Additional supporting information may be found in the online version of the article at the publisher's website.

Figure S1. Smith charts and reflection plots for all tested combinations of the length ℓ and gap position d, evaluated for a range of inductor values L. Each row represents a specific antenna length, while each column shows a different gap position. For every combination of these, the dependence of reflection and impedance on L is investigated.

Figure S2. (A) Three setups for measurements to show the effect of cable-coil coupling. Top: The feeding cable is routed perpendicularly and away to the antenna. Middle: the feeding cable is routed parallel to the antenna and is placed directly on the side of the housing of the antenna. Bottom: The feeding cable is routed parallel to the antenna and is placed directly on the housing of the antenna (worst case scenario). (B) B_1^+ maps for the three situations. (AFI[19] with FA/TE/TR1/TR2 = 65°/2.6/50/250 ms). These B_1^+ maps show that the distribution changes when the antenna is closer to the feeding cable.

How to cite this article: Budé LMI, Steensma BR, Zivkovic I, Raaijmakers AJE. The coax monopole antenna: A flexible end-fed antenna for ultrahigh field transmit/receive arrays. *Magn Reson Med*. 2024;92:361-373. doi: 10.1002/mrm.30036